Nonlinear earthquake response of marine sediments with distributed acoustic sensing

Loïc Viens[1], Luis Fabian Bonilla[2], Zack J. Spica[1], Kiwamu Nishida[3], Tomoaki Yamada[3], Masanao Shinohara[3]

[1]Department of Earth and Environmental Sciences, University of Michigan, Ann Arbor, Michigan, USA
[2]Department of Geotechnical Engineering, Environment, Natural hazards and Earth sciences, Université Gustave Eiffel, Marne-la-Vallée, France
[3]Earthquake Research Institute, The University of Tokyo, Tokyo, Japan

Key Points:

- AutoCorrelation Functions (ACFs) of earthquakes recorded by Distributed Acoustic Sensing (DAS) exhibit phase delays during ground motions
- ACF time delays are converted to relative velocity drops in the medium, which characterize soil non-linearity
- DAS is used to infer the nonlinear behavior of soils with an unprecedented spatial resolution

Corresponding author: Loïc Viens, `lviens@umich.edu`

Abstract

Seismic waves can be significantly amplified by soft sediment layers. Large dynamic strains can trigger a nonlinear response of shallow soils having low strength, which is characterized by a shift of the resonance frequencies, ground motion deamplification, and in some cases, soil liquefaction. We investigate the response of marine sediments during earthquake ground motions recorded along a fiber-optic cable offshore the Tohoku region, Japan, with Distributed Acoustic Sensing (DAS). We compute AutoCorrelation Functions (ACFs) of the ground motions from 103 earthquakes in different frequency bands. We detect time delays in the ACF waveforms that are converted to relative velocity changes (dv/v). dv/v drops, which are characteristic of soil nonlinearity, are observed during the strongest ground motions. Moreover, the dv/v values show a strong variability along the cable. This study demonstrates that DAS can be used to infer the dynamic properties of the shallow Earth with an unprecedented spatial resolution.

Plain Language Summary

Seismic waves from earthquakes are amplified by shallow and soft sediment layers of the Earth. This amplification is linear for weak seismic waves, but can become highly nonlinear during strong ground motions. Nonlinear soil response, which can lead to a complete failure of the ground through soil liquefaction, threatens the safety of human-made constructions and needs to be accurately characterized. We study the response of marine sediments offshore the Tohoku region in Japan using earthquake data recorded along 43.3 km of a fiber-optic cable with Distributed Acoustic Sensing (DAS). We use an autocorrelation approach to analyze the ground motions from 103 earthquakes recorded by thousands of DAS channels. We detect a clear nonlinear behavior of shallow sediments during the strongest ground motions. Moreover, we show that soil nonlinearity significantly varies along the cable. Our methodology could easily be applied to earthquake DAS data recorded in populated and seismically active regions to help better understanding the dynamic behavior of shallow soils.

1 Introduction

Local geological conditions can significantly impact the propagation of incoming seismic waves from earthquakes. In particular, shallow, soft, and unconsolidated sediment layers are well known to amplify earthquake ground motions (Sanchez-Sesma, 1987), which can lead to catastrophic events such as during the 1985 moment magnitude (M_w) 8.0 Michoacán earthquake in Mexico (Anderson et al., 1986; Campillo et al., 1989). When subjected to weak dynamic strains (i.e., less than 10^{-4} and 10^{-8} for field observations and laboratory experiments, respectively; Ishihara, 1996; TenCate et al., 2004), shallow soils linearly amplify seismic waves. During large dynamic strains, however, soft sediments can behave nonlinearly (e.g., Field et al., 1997; Ostrovsky & Johnson, 2001). Soil nonlinearity is generally characterized by a relative reduction of the high-frequency ground-motion amplification, which is related to an increase of damping in the medium, and a shift of the resonance frequency to lower frequencies due to a reduction of the shear modulus (Beresnev & Wen, 1996; Brunet et al., 2008; Bonilla et al., 2011; Lyakhovsky et al., 2009; Zaitsev et al., 2005). In some cases, large dynamic strains can trigger a complete failure of cohesionless and saturated shallow sediments through soil liquefaction (Kramer, 1996), which can have disastrous consequences for human infrastructures as observed during the 1964 Niigata (Japan, Ohsaki, 1966) and 2010–2011 Christchurch (New Zealand, Quigley et al., 2013) earthquakes. Therefore, characterizing the nonlinear response of shallow sediments to earthquake ground motions is critical for better mitigating seismic risk.

Several empirical methods have been developed to assess the response of soils to ground motions. A classical approach relies on computing the spectral ratio of earthquakes recorded at a soft-soil site and at a nearby reference rock site (Borcherdt, 1970; Field & Jacob, 1995; Bonilla et al., 1997). However, this method suffers from the fact that a reference site may not always be available in the vicinity of the site of interest. Another approach consists in using pairs of surface-borehole stations to detect potential soil non-linear elastic behavior between the two sensors (Bonilla et al., 2011; Minato et al., 2012; Nakata & Snieder, 2011; Régnier et al., 2013; Sawazaki et al., 2006; Takagi et al., 2012; Wen et al., 1995). While this technique allows us to isolate the shallow subsurface response from the earthquake source and path effects, pairs of surface-borehole instruments are expensive to install and their low spatial coverage prevents us from capturing small-scale lateral variations.

AutoCorrelation Functions (ACFs) calculated from data recorded by surface seismometers yield the reflectivity response of the underlying elastic structure (Claerbout, 1968; Wapenaar, 2003). This technique has been primarily applied to image interfaces with strong seismic impedance contrasts using earthquake (Delph et al., 2019; Pham & Tkalčić, 2017; Tork Qashqai et al., 2019; Viens, Jiang, & Denolle, 2022) and ambient seismic field (ASF; Gorbatov et al., 2013; Ito et al., 2012; Kennett, 2015; Saygin et al., 2017; Spica et al., 2020; Viens, Jiang, & Denolle, 2022) datasets. Repeated ACF computations through time from continuous ASF time series have also been used to monitor temporal seismic velocity changes in the subsurface in different environments, such as volcanic (De Plaen et al., 2016; Sens-Schönfelder & Wegler, 2006; Yates et al., 2019) and earthquake source (Hobiger et al., 2014; Ohmi et al., 2008; Wegler et al., 2009) regions. However, the partitioning of surface and body waves in ACFs computed from the ASF is generally unknown and hinders the interpretation of the measured velocity changes (Nakahara, 2015). To ease the interpretation, ACFs have also been computed from earthquake P-, S-, or coda-wave windows (Bonilla et al., 2019; Bonilla & Ben-Zion, 2020; Nakahara, 2015; Qin et al., 2020). Bonilla and Ben-Zion (2020) showed that the first negative peak of ACFs calculated during earthquake ground motions corresponds to the seismic-wave two-way travel time between the sensor and the first major interface below the station, and captures the soil non-linear response. Moreover, Bonilla et al. (2019) and Qin et al. (2020) showed that the response of the shallow subsurface obtained from ACFs at surface stations yields a similar estimation of the soil nonlinear behavior as that from a surface-borehole station configuration. In other words, ACFs can isolate the site response term from the earthquake source and path effects, which makes single-component stations a powerful tool to analyze shallow sediment nonlinear behavior.

Mapping local site effects with data-driven techniques remains challenging due to the large density of seismometers needed to capture complex spatial variations of the seismic wavefield. In some cases, a large station coverage can be nearly impossible to attain due to environmental or physical constrains, especially in urban and underwater areas. Nevertheless, recent technological advances in Distributed Acoustic Sensing (DAS) offer an unprecedented opportunity to measure the Earth's vibrations over tens of kilometers with a dense spatial resolution ($\sim$1–10 m) by turning ground-coupled fiber-optic cables into arrays of sensors (Hartog, 2017). DAS uses an optoelectrical interrogator to probe fibers with a laser sending thousands of short pulses of light every second. As each pulse of light travels down the fiber, some of the light is reflected back to the interrogator in a process known as Rayleigh backscatter. External forcing, such as seismic waves, generate phase shifts of the back-scattered Rayleigh light, which are measured by the interrogator. The measured phase shifts are finally linearly converted to longitudinal strain (or strain-rate) along the cable over a sliding spatial distance (i.e., the gauge length). Both fit-to-purpose and existing telecommunication fiber-optic cables have been used to record high-fidelity earthquake wavefields (Lellouch et al., 2019; Spica et al., 2022; Wang et al., 2018; Zeng et al., 2017). One great advantage of telecommunication fibers is that they have been widely deployed, from the oceans' bottom to nearly every street in large developed cities, to sustain our modern telecommunication network. Therefore, DAS could complement expensive urban and offshore seismic array deployments by probing existing telecommunication cables to capture the full extent of earthquake wavefields.

In this study, we analyze the response of shallow marine sediments to 103 earthquakes recorded along a telecommunication cable offshore the Sanriku coast in Japan by a DAS experiment (Figures 1a–b). We calculate ACFs from the earthquake ground motions after filtering the data into different frequency bands to infer the soil response at different depths. We detect changes in the ACF time series that are converted to relative velocity changes to characterize the soil linear and nonlinear regimes below each DAS channel. We show that the relative velocity changes exhibit spatial variations along the cable which are strongly influenced by the ACF frequency ranges. We finally discuss our results and the potential of DAS for extracting soil parameters with an unprecedented spatial resolution.

2 Data and Methods

2.1 DAS data

The Earthquake Research Institute, The University of Tokyo, operates an ocean-bottom observatory composed of three 3-component accelerometers and two tsunami meters offshore the Sanriku Coast (Figure 1b; Kanazawa & Hasegawa, 1997; Shinohara et al., 2021, 2022). The data recorded by the instruments are streamed in real-time to the landing station located in the city of Kamaishi through a submarine telecommunication cable. The cable contains six dark (unused) dispersion-shifted single-mode optical fibers with a wavelength of 1,550 nm, which are suitable for DAS measurements. Moreover, the first 47.7 km of the cable are relatively straight and are buried under 0.6-0.7 m of sediments, which guarantees a good coupling of the fiber.

An AP Sensing N5200A DAS interrogator unit (Cedilnik et al., 2019) probed one of the dark fibers between November 18 and December 2, 2019, and recorded continuous data over the first 70-km of the cable with a sampling rate of 500 Hz. The gauge length and spatial sampling are set to 40 m and 5.1 m, respectively. During the two weeks of measurement, hundreds of earthquakes were recorded by the DAS system. We first convert the raw DAS data to strain (Shinohara et al., 2022) and focus on the ground motions from 103 earthquakes that were clearly recorded by all the DAS channels (Figure 1a-b). The velocity magnitude (M_V) of the earthquakes ranges between 1.0 and 6.3, and we show the strain waveforms of a M_V 2.5 earthquake in Figure 1c. This event occurred on November 28, 2019 at 14:17:32UTC at a depth of 30 km. Clear P- and S-wave arrivals can be observed at most channels as well as locally generated surface waves which significantly extend the ground motion duration.

2.2 Autocorrelation functions and relative velocity changes

For each earthquake and each DAS channel, we compute the time derivative of the strain data to retrieve strain-rate waveforms, which are proportional to acceleration time series. We then bandpass filter the strain-rate data between 2 and 30 Hz (all filters are two-pass four-pole Butterworth bandpass filters) and select a fixed 15-s window starting 5 s before the earthquake absolute maximum amplitude. We then further bandpass filter the strain-rate waveforms into 19 frequencies bands (e.g., 2-4, 3-6,..., 20-40 Hz) and compute ACFs over the fixed 15-s window using the phase correlation method in the frequency domain (Schimmel & Paulssen, 1997; Ventosa et al., 2019). We show the bandpass filtered strain-rate waveforms of the M_V 2.5 earthquake together with their corresponding ACFs at channel 5000 in Figures 1d and 1e, respectively. The ACFs are calculated around the S-wave direct arrival and we therefore expect their first negative peak to capture the S-wave two-way travel time (Bonilla & Ben-Zion, 2020). Moreover, the different frequency bands allow us to sample different depth of the media, with low-frequency

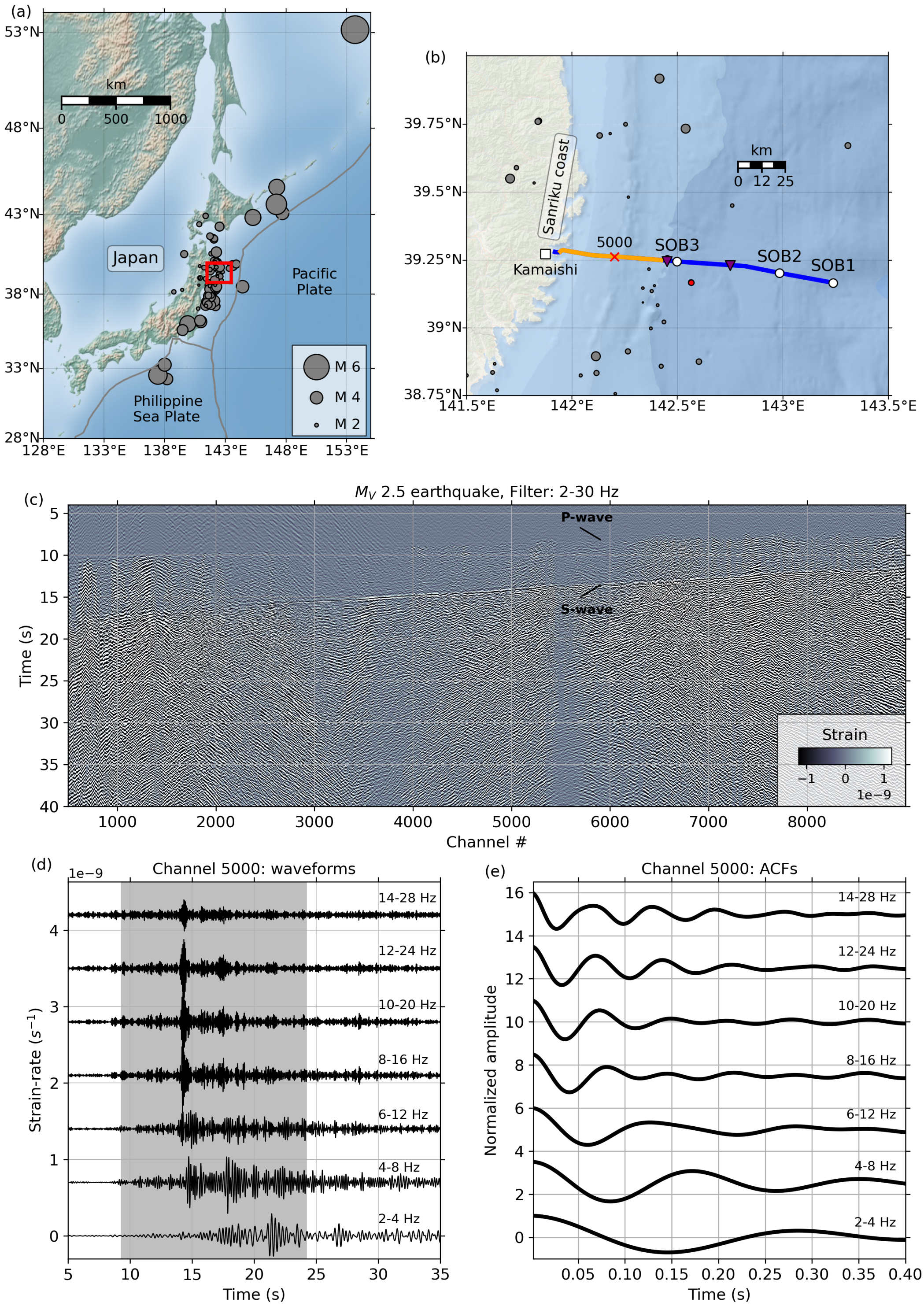

Figure 1. (a) Topographic map of the Japanese Islands and their surroundings including the 103 earthquakes used in this study. The red rectangle denotes the region near the cable shown in (b). (b) Bathymetric map offshore the Sanriku coast including the location of the seafloor cable observation system. The orange line denotes the buried section of the cable used in this study (i.e., channels 500 to 9000) and the location of channel 5000 is indicated by the red cross. The white circles and purple inverted triangles show the positions of the accelerometers and tsunamimeters, respectively. The location of the velocity magnitude (M_V) 2.5 event (red circle) shown in (c) and that of other nearby earthquakes (gray circles) are highlighted. The magnitude scale is the same as in (a). (c) Strain waveforms of the M_V 2.5 event bandpass filtered between 2 and 30 Hz between channels 500 and 9000. The waveform amplitudes are clipped for visibility. (d) Strain-rate waveforms of the M_V 2.5 earthquake bandpass filtered in different frequency bands at channel 5000. The gray area denotes the time period over which ACFs are calculated. (e) Amplitude normalized ACFs computed from the waveforms shown in (d).

bandpass filtered ACFs displaying later arrivals as they sample deeper media compared to high-frequency ACFs.

The 103 earthquake waveforms analyzed in this study generated various levels of dynamic strain along the cable. In Figures 2a-d, we show the ACFs calculated for all the earthquakes after bandpass filtering the strain-rate data in the 10–20 Hz and 15–30 Hz frequency bands at channels 5000 and 7000. We also show the dynamic peak strains computed as the maximum absolute amplitude of the bandpass filtered strain data in Figures 2e-f. For both frequency bands, the ACF first negative peaks exhibit similar lag-times for weak dynamic strains (e.g., less than $\sim 5\times10^{-10}$), but clear delays can be observed for larger dynamic peak strains.

Soil nonlinear behavior during ground motions delays the ACF first negative peak and can therefore be interpreted as a velocity reduction of the medium (Bonilla & Ben-Zion, 2020). Under the assumption that the changes in the medium are uniformly distributed, we can estimate the relative velocity changes (dv/v) of each ACF with respect to a reference ACF with the stretching method (Lobkis & Weaver, 2003; Sens-Schönfelder & Wegler, 2006) as

$$\tau = \frac{dt}{t} = -\frac{dv}{v}, \tag{1}$$

where τ, dt/t, and dv/v are the stretching coefficient, the relative time shift, and the relative velocity change, respectively. For each channel and each frequency band, we first compute a reference ACF by stacking the ACFs from the earthquake waveforms that generated the ten weakest dynamic peak strains. For each frequency band, we then select a time window that corresponds to 75% of the inverse of the lower cutoff frequency (e.g., the first 0.375 s of the ACF for the 2-4 Hz frequency band) to focus on the first negative peak of the ACFs. We then stretch and compress the selected window of the reference ACF to find the stretching coefficient that maximizes the fit between the reference and each ACF waveform, and therefore infer relative velocity changes. The stretching is performed in two steps; we first use ten values uniformly distributed between -50 and 50% of stretching to find an initial guess of the stretching coefficient, and then refine the measurement by interpolating the stretched waveforms 500 times between the neighboring values (similar to Viens et al., 2018).

3 Results

We show the relative velocity changes for all the frequency bands and earthquakes for two ranges of channels in Figures 3a-b. While the soil nonlinear response can rapidly evolve spatially, we display the combined results at 10 neighboring channels (i.e., over 51 m) between channels 5000–5010 and 7000–7010 for visibility. For dynamic peak strains smaller than $\sim 5\times10^{-10}$, dv/v measurements are generally equal to zero for all the frequency bands at both locations, which indicates that there is no change in the medium. However, clear dv/v drops can be observed in different frequency bands at the two locations with increasing dynamic peak strains. For example, we primarily observe dv/v reductions between central frequencies (i.e., the central frequency of the bandpass filter; 15 Hz for the 10–20 Hz bandpass filter) of 15–24 Hz for channels 5000–5010 and between 12–28 Hz for channels 7000–7010. Moreover, we also note that the intensity of the dv/v changes varies, with larger changes observed at channels 5000–5010 compared to those at channels 7000–7010.

Spatial variations of the relative velocity changes can also be tracked along the cable thanks to the high density of DAS channels. In Figures 3c-d, we show the relative velocity changes along the cable in two frequency bands (e.g., 5–10 and 10–20 Hz). Clear differences can be observed between the two frequency ranges. In the 5–10 Hz frequency band, almost no dv/v changes can be observe between channels 500 and 6900, even during the strongest dynamic peak strains. However, we detect clear dv/v drops for dynamic

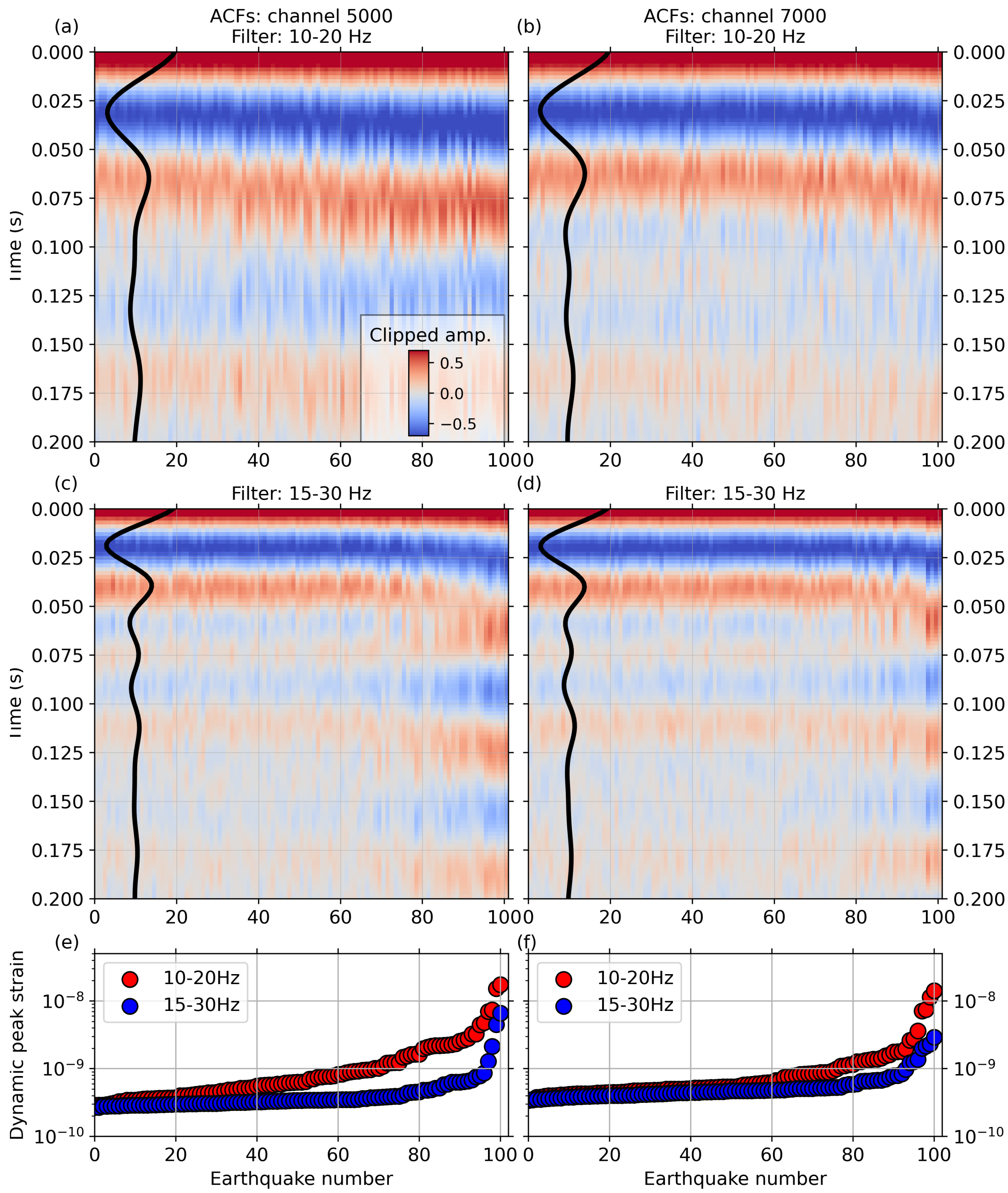

Figure 2. (a) ACFs computed from the 103 earthquakes bandpass filtered between 10 and 20 Hz at channels (a) 5000 and (b) 7000. The amplitude of the data is clipped for visibility. (c–d) Same as (a–b) for the data bandpass filtered between 15 and 30 Hz. In (a–d), the ACFs are sorted by increasing dynamic peak strain values, which are computed after bandpass filtering the strain waveforms in their respective frequency bands. (e–f) Dynamic peak strains after bandpass filtering the earthquake waveforms between 10–20 Hz and 15–30 Hz at channels 5000 and 7000, respectively.

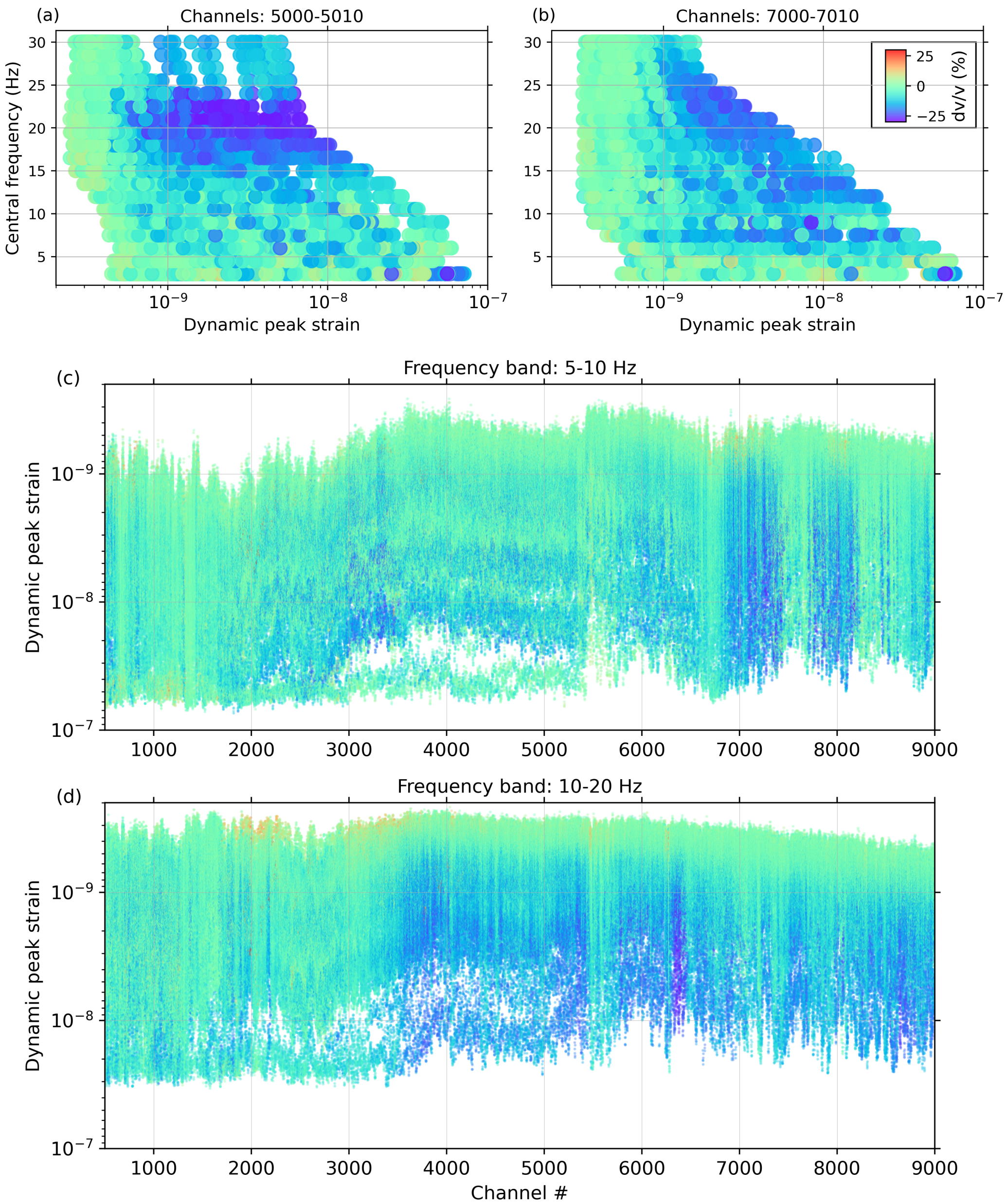

Figure 3. (a) dv/v measurements at channels 5000–5010 for the 19 frequency bands and the 103 earthquakes. Dynamic peak strains are computed for each event and each station after bandpass filtering the strain data. The central frequency corresponds to the central frequency of the bandpass filter (e.g., 15 Hz for the 10–20 Hz bandpass filter). (b) Same as (a) at channels 7000–7010. (c) dv/v measurements from the ACFs computed from the 103 earthquakes bandpass filtered between 5 to 10 Hz between channels 500 and 9000 as a function of the dynamic peak strain. (d) Same as (c) for the 10–20 Hz frequency band. The dv/v color-scale shown in (b) is the same for all panels.

peak strains above 10^{-9} between channels 6900 and 8200. In the 10–20 Hz frequency band, almost no changes are found between channels 500–3500, but large dv/v drops are observed after channels 3500 for dynamic peak strains larger than $\sim 10^{-9}$.

To isolate and investigate the average sediment response during strong ground motions, we also compute dv/v measurements between each reference ACF (i.e., the stack of the ACFs computed during the 10 weakest dynamic peak strains) and a stack of the ACFs computed during the five largest dynamic peak strains. dv/v changes between weak and strong ground motion ACFs exhibit clear spatial and frequency variations (Figure 4a). Between channels 500 and 2000, we do not observe any large dv/v changes in any frequency band. However, we observe spatial variations of the dv/v reductions at central frequencies above 15 Hz between channels 2000 and 9000. We also observe clear dv/v changes at frequencies below 15 Hz between channels 6300 and 9000. Such coherent spatial changes across frequency bands highlight the sensitivity of DAS ACFs to local site conditions as well as their depth sensitivities.

The amplitude of dv/v reductions is expected to increase with increasing dynamic peak strains. In Figure 4b-d, we show the dv/v measurements calculated between the weak and strong ground motion ACFs as a function of the dynamic peak strains in three frequency bands. We only show the results at 650 locations between channels 1700-8200 as we average the dv/v and dynamic peak strain values over 10 neighboring channels (e.g., channels 1995-2005 for channel 2000). This step is perform to compare our results with local site condition data from a velocity model of the region, as discussed below. In the 2–4 and 20–40 Hz, the largest dv/v drops correlate with the channels where the largest dynamic peak strains are recorded, typically near the beginning of the cable. In the 15–30 Hz frequency band, however, dv/v changes are almost constant between dynamic peak strains of 10^{-9} and $2{\times}10^{-8}$ with an average value of -20%. This suggests that the nonlinearity threshold in this frequency range is lower than dynamic peak strains of 10^{-9}.

In Figures 4e–g, we show the dv/v measurements at the same 650 locations along the cable as a function of the average S-wave velocity in the first 30 m of the ground (V_{S30}) obtained from the velocity model derived by Viens, Perton, et al. (2022). The Viens, Perton, et al. (2022) model was obtained by inverting Rayleigh-wave phase velocity dispersion curves calculated by seismic interferometry using virtual sources located every 10 channels (e.g., 51 m). We compute V_{S30} from the 650 locations of the velocity model and apply a smoothing of the V_{S30} values over 5 locations. We observe a decrease of the dv/v values with decreasing V_{S30} values in the 2-4 Hz and 20-40 Hz frequency band. However, we do not observe any correlation between V_{S30} and the dv/v results in the 10-20 Hz frequency band. Nevertheless, the correlation between dv/v values and V_{S30} is relatively weak, which suggests that V_{S30} is not the best parameter to characterize the nature of soil nonlinearity as also shown by Bonilla et al. (2021).

4 Discussion

While larger dynamic peak strains generally correlate with larger dv/v drops, the correlation with V_{S30} is weaker or even nonexistent. Three hypotheses can explain this behavior. First, the velocity model, which was obtained from ASF cross-correlation functions spanning over 2 km (i.e., 400 channels), only captures a smoothed representation of the shallow Earth structure. Therefore, the V_{S30} parameter extracted from the velocity model may not fully capture the structural changes that can rapidly occur at shallow depth. Secondly, we expect the ACFs to have different depth sensitivities based of their frequency ranges. Therefore, a single parameter, namely V_{S30}, does not account for such depth sensitivity variations. Thirdly, while an accurate value of V_{S30} can be useful for some geotechnical engineering purposes, it may not be the best parameter to explain the intensity of the dv/v drops. For example, in a 30 m profile composed of a very shallow and soft sediment layer overlaying a stiffer material, nonlinearity is expected to

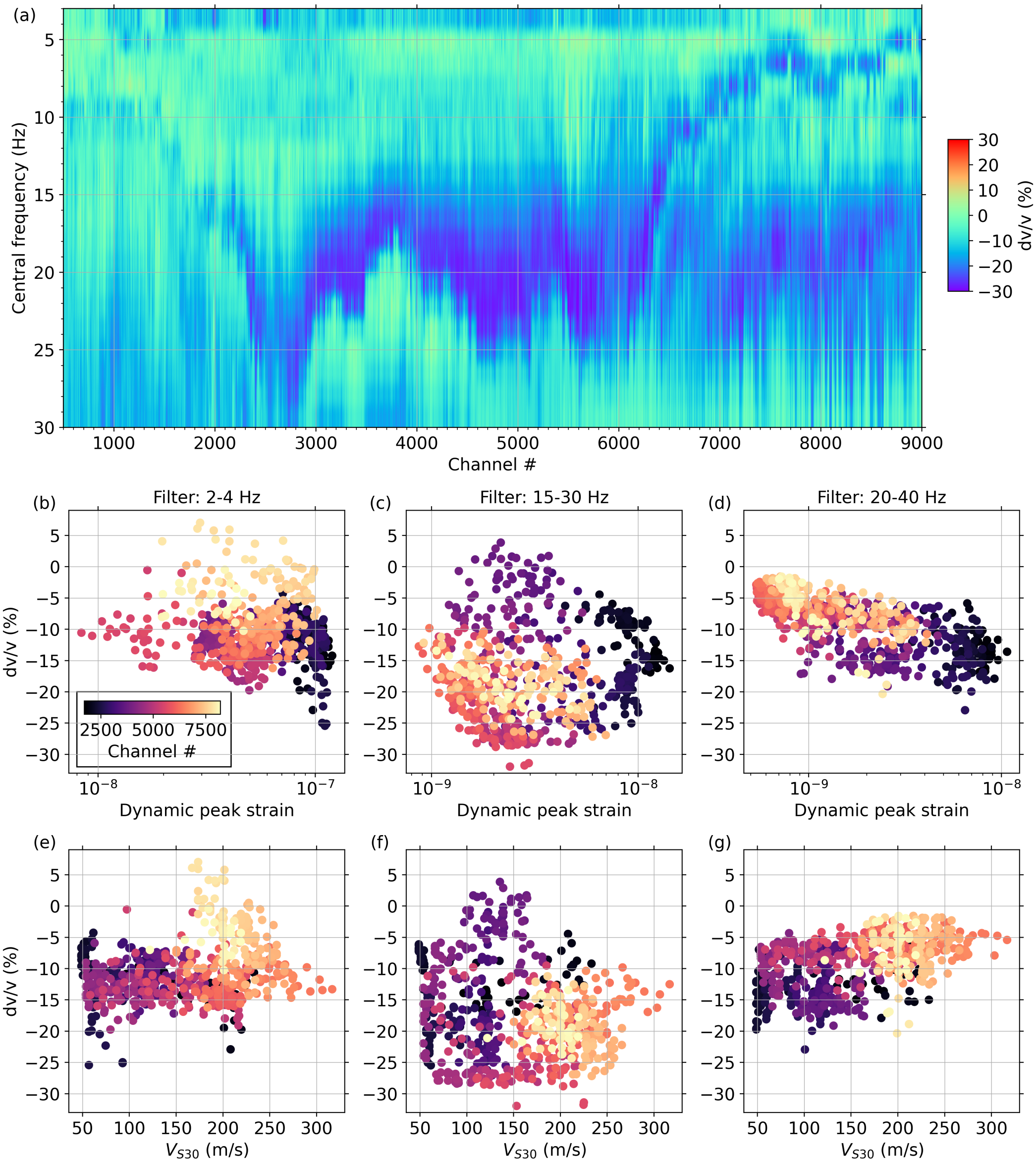

Figure 4. (a) dv/v measurements computed between a reference ACF, which represents the soil linear response, and average ACF obtained from the earthquakes that generated the five largest peak strains, which captures the nonlinear behavior of sediments, at each channel and each frequency band. (b) Relative velocity changes as a functions of the filtered dynamic peak strain in the 2-4 Hz frequency bands. (c–d) Same as (b) for the 10-20 and 20-40 Hz frequency bands. (e) Relative velocity changes as a function of the average S-wave velocity within the first 30 m of the ground (V_{S30}) for the 2-4 Hz frequency bands. (f–g) Same as (g) for the 10-20 and 20-40 Hz frequency bands. In (b–g), the color-bar corresponds to the channel number.

only occur in the first layer. Therefore, a complete velocity profile of each site is likely to be more informative than a summarizing parameter such as V_{S30} (Bonilla et al., 2021), and future work should focus on refining the shallow structure of the velocity model.

While the recorded dynamic strains from the earthquakes considered in this study are relatively weak, we observe significant relative velocity changes from the ACFs, which indicate a nonlinear response of marine sediments. Due to the weak levels of shaking, the soil nonlinear behavior only occurs during the passing of seismic waves, and no long-term effects, as those observed at land stations after the 2011 M_w 9.0 Tohoku-Oki earthquake (Bonilla et al., 2021), could be detected. Nevertheless, the nonlinearity thresholds of strain levels obtained along the cable are consistent with those from laboratory experiments (Pasqualini et al., 2007; Remillieux et al., 2017; TenCate et al., 2004) and from ACFs computed from a seismic array in California (Bonilla & Ben-Zion, 2020). To further validate our approach, we also compute ACFs from earthquake data recorded by the horizontal accelerometer along the axis of the cable from the SOB3 station (Figure 1b). ACFs are computed for the same earthquakes as for the DAS dataset as well as 138 nearby M_w 5+ earthquakes which occurred between 2015 and 2021 (Figure S1). The ACFs from the SOB3 station exhibit similar features, with a nonlinearity threshold of the same order as that obtained with the DAS data, which validates our approach.

The dynamic peak strain recorded by the DAS channels are in the direction of the cable. However, DAS has different theoretical sensitivities depending on the type of seismic waves and their incidence angles (Martin et al., 2021). For example, DAS records from earthquakes occurring at a 90 degree angle from the direction of the cable are expected to exhibit less energy than events happening along the axis of the cable. Moreover, the relatively long gauge length (e.g., 40 m) used to record the DAS data could potentially create notches in the frequency spectrum between 2 and 40 Hz (Dean et al., 2017). Nevertheless, the steep subduction zone in the Tohoku region (Hayes et al., 2018) combined to shallow and slow sediment layers interfere with the propagation of seismic waves, which likely arrive with almost vertical angles to the cable. This translates into high apparent velocities of all earthquake wavefields recorded by the cable (e.g., Figure 1c), which limits both the azimuthal and gauge length effects on the recorded data. We further confirm this point by comparing the maximum amplitudes of DAS and SOB3 data during the 103 earthquakes considered in this study in Figure S2. Both datasets exhibit similar maximum amplitudes with respect to azimuth angles to the earthquake epicenters, which confirms that there is no noticeable azimuthal effect for the DAS data.

The largest ground motions during the two week experiment occurred during a M_V 5.6, which occurred 50 km east of the SOB3 station (Figure S3). Unfortunately, the data recorded by the DAS system clipped and are therefore not usable in our analysis. The clipping of the data is caused by rapid phase changes that occurred during strong ground motions, which wraps the signal's phase. To reduce clipping effects and improve the dynamic range of DAS experiments, one can increase the laser's pulse rate frequency, which would limit the maximum distance that can be sampled by the DAS system, and/or reduce the gauge length, which could result in a decrease of the SNR of the recorded wavefield (Mellors et al., 2022). Despite these drawbacks, a better tuning of the DAS parameters could allow us to record strong ground motions that are likely to trigger stronger nonlinear soil responses.

5 Conclusions

We analyzed the ground motions of 103 earthquakes recorded along a fiber-optic cable during a two-week DAS campaign offshore the Tohoku region, Japan. We computed ACFs of earthquake ground motions and detected relative velocity changes in the marine sediments surrounding the cable from the ACFs. Large drops of dv/v are observed along the cable and are typical of a nonlinear behavior of the medium. Moreover, the

dv/v changes are frequency and spatially dependent, which highlights the sensitivity of DAS ACFs to the shallow Earth structure.

This study demonstrates that earthquakes recorded by DAS can be used to characterize the nonlinear behavior of soils during ground motions. This characterization could be of critical importance for fiber-optic cables used for earthquake early warning purposes as soil nonlinearity impacts the amplitude and frequency content of the recorded wavefield, and could bias rapid magnitude estimations. Nevertheless, the ACF approach could easily be applied to other DAS datasets recorded in populated regions located on top of sedimentary basins, such as Mexico City and Los Angeles, to better characterize seismic hazard.

Acknowledgments

We thank Takeshi Akuhara for providing useful information about DAS measurements. We thank *Fujitsu* for cooperating with the Earthquake Research Institute (ERI), The University of Tokyo, for the DAS measurement campaigns. All the Figures are plotted with Matplotlib (Hunter, 2007). Some of the data processing steps have been performed using ObsPy (Beyreuther et al., 2010). **Funding:** This project was partly supported by the discretionary budget of the director of ERI. The observations were carried out as part of the Earthquake and Volcano Hazards Observation and Research Program by the Ministry of Education, Culture, Sports, Science, and Technology of Japan. L.V. is supported by NSF award EAR2022716. Z.J.S acknowledges support from the Air Force Research Laboratory grant FA9453-21-2-0018. **Competing interests:** The authors declare that they have no competing interests. **Data availability:** The codes developed to perform the technical analysis and to reproduce most figures are available at `https://doi.org/10.5281/zenodo.6672479`.

References

Anderson, J. G., Bodin, P., Brune, J. N., Prince, J., Singh, S. K., Quaas, R., & Onate, M. (1986). Strong ground motion from the Michoacan, Mexico, earthquake. *Science*, *233*, 1043–1049. doi: 10.1126/science.233.4768.1043

Beresnev, I. A., & Wen, K.-L. (1996). Nonlinear soil response—a reality? *Bull. Seismol. Soc. Am.*, *86*, 1964–1978. Retrieved from `http://bssa.geoscienceworld.org/content/86/6/1964`

Beyreuther, M., Barsch, R., Krischer, L., Megies, T., Behr, Y., & Wassermann, J. (2010, 05). ObsPy: A Python Toolbox for Seismology. *Seism. Res. Lett.*, *81*(3), 530-533. Retrieved from `https://doi.org/10.1785/gssrl.81.3.530` doi: 10.1785/gssrl.81.3.530

Bonilla, L. F., & Ben-Zion, Y. (2020, 11). Detailed space–time variations of the seismic response of the shallow crust to small earthquakes from analysis of dense array data. *Geophys. J. Int.*, *225*(1), 298-310. Retrieved from `https://doi.org/10.1093/gji/ggaa544` doi: 10.1093/gji/ggaa544

Bonilla, L. F., Guéguen, P., & Ben-Zion, Y. (2019, 01). Monitoring Coseismic Temporal Changes of Shallow Material during Strong Ground Motion with Interferometry and Autocorrelation. *Bulletin of the Seismological Society of America*, *109*(1), 187-198. doi: 10.1785/0120180092

Bonilla, L. F., Guéguen, P., & C., G. (2021, 30 August–1 September). Contribution of k-net and kik-net data to the monitoring of nonlinear properties of the shallow crust. In *6th iaspei/iaee international symposium: Effects of surface geology on seismic motion.* Kyoto, Japan. Retrieved from `http://www.esg6.jp`

Bonilla, L. F., Steidl, J. H., Lindley, G. T., Tumarkin, A. G., & Archuleta, R. J. (1997). Site amplification in the san fernando valley, california: Variability of site-effect estimation using the s-wave, coda, and h/v methods. *Bull. Seismol. Soc. Am.*, *87*, 710. Retrieved from `+http://dx.doi.org/`

Bonilla, L. F., Tsuda, K., Pulido, N., Régnier, J., & Laurendeau, A. (2011). Nonlinear site response evidence of K-NET and KiK-net records from the 2011 off the Pacific coast of Tohoku Earthquake. *Earth Planets Space*, *63*, 785–789. Retrieved from `http://dx.doi.org/10.5047/eps.2011.06.012` doi: 10.5047/eps.2011.06.012

Borcherdt, R. D. (1970). Effects of local geology on ground motion near san francisco bay. *Bull. Seismol. Soc. Am.*, *60*, 29. Retrieved from `+http://dx.doi.org/`

Brunet, T., Jia, X., & Johnson, P. A. (2008). Transitional nonlinear elastic behaviour in dense granular media. *Geophys. Res. Lett.*, *35*, L19308. Retrieved from `https://agupubs.onlinelibrary.wiley.com/doi/abs/10.1029/2008GL035264` doi: 10.1029/2008GL035264

Campillo, M., Gariel, J. C., Aki, K., & Sánchez-Sesma, F. J. (1989). Destructive strong ground motion in Mexico city: Source, path, and site effects during great 1985 Michoacán earthquake. *Bull. Seismol. Soc. Am.*, *79*, 1718–1735. Retrieved from `http://www.bssaonline.org/content/79/6/1718.abstract`

Cedilnik, G., Lees, G., Schmidt, P., Herstrøm, S., & Geisler, T. (2019). Ultra-long reach fiber distributed acoustic sensing for power cable monitoring. *10th International Conference on Insulated Power Cables*. Retrieved from `https://www.apsensing.com/fileadmin/Publication%20Files/Cedilnik_et_al._-_2019-Jicable-Proceedings-E4-4-Ultralong-reach-DAS-.pdf`

Claerbout, J. (1968). Synthesis of a layered medium from its acoustic transmission response. *Geophysics*, *33*, 264–269. doi: 10.1190/1.1439927

Dean, T., Cuny, T., & Hartog, A. H. (2017). The effect of gauge length on axially incident p-waves measured using fibre optic distributed vibration sensing. *Geophysical Prospecting*, *65*(1), 184-193. Retrieved from `https://onlinelibrary.wiley.com/doi/abs/10.1111/1365-2478.12419` doi: https://doi.org/10.1111/1365-2478.12419

Delph, J. R., Levander, A., & Niu, F. (2019). Constraining crustal properties using receiver functions and the autocorrelation of earthquake-generated body waves. *Journal of Geophysical Research: Solid Earth*, *124*(8), 8981–8997. doi: 10.1029/2019JB017929

De Plaen, R. S. M., Lecocq, T., Caudron, C., Ferrazzini, V., & Francis, O. (2016). Single-station monitoring of volcanoes using seismic ambient noise. *Geophys. Res. Lett.*, *43*, 8511–8518. Retrieved from `http://dx.doi.org/10.1002/2016GL070078` doi: 10.1002/2016GL070078

Field, E. H., & Jacob, K. H. (1995, 08). A comparison and test of various site-response estimation techniques, including three that are not reference-site dependent. *Bull. Seismol. Soc. Am.*, *85*, 1127-1143. Retrieved from `https://doi.org/10.1785/BSSA0850041127` doi: 10.1785/BSSA0850041127

Field, E. H., Johnson, P. A., Beresnev, I. A., & Zeng, Y. (1997, 12 11). Nonlinear ground-motion amplification by sediments during the 1994 northridge earthquake. *Nature*, *390*, 599-602. Retrieved from `http://dx.doi.org/10.1038/37586`

Gorbatov, A., Saygin, E., & Kennett, B. L. N. (2013, 12). Crustal properties from seismic station autocorrelograms. *Geophys. J. Int.*, *192*(2), 861-870. doi: 10.1093/gji/ggs064

Hartog, A. (2017). *An introduction to distributed optical fibre sensors*. CRC Press. doi: https://doi.org/10.1201/9781315119014

Hayes, G. P., Moore, G. L., Portner, D. E., Hearne, M., Flamme, H., Furtney, M., & Smoczyk, G. M. (2018). Slab2, a comprehensive subduction zone geometry model. *Science*, *362*(6410), 58-61. Retrieved from `https://www.science.org/doi/abs/10.1126/science.aat4723` doi: 10.1126/science.aat4723

Hobiger, M., Wegler, U., Shiomi, K., & Nakahara, H. (2014). Single-station cross-correlation analysis of ambient seismic noise: application to stations in the surroundings of the 2008 iwate-miyagi nairiku earthquake. *Geophys. J. Int.*, *198*, 90. Retrieved from +http://dx.doi.org/10.1093/gji/ggu115 doi: 10.1093/gji/ggu115

Hunter, J. D. (2007). Matplotlib: A 2d graphics environment. *Computing In Science & Engineering*, *9*(3), 90–95. doi: 10.1109/MCSE.2007.55

Ishihara, K. (1996). *Soil behaviour in earthquake geotechnics.* Clarendon Press. Retrieved from https://books.google.com/books?id=OXNxQgAACAAJ

Ito, Y., Shiomi, K., Nakajima, J., & Hino, R. (2012). Autocorrelation analysis of ambient noise in northeastern Japan subduction zone. *Tectonophysics*, *572-573*, 38 - 46. doi: https://doi.org/10.1016/j.tecto.2011.09.019

Kanazawa, T., & Hasegawa, A. (1997). Ocean-bottom observatory for earthquakes and tsunami off sanriku, north-east japan using submarine cable. *International Workshop on Scientific Use of Submarine Cables, Comm. for Sci. Use of Submarine Cables, Okinawa, Japan, 1997*, 208-209. Retrieved from https://ci.nii.ac.jp/naid/10030183328/en/

Kennett, B. (2015). Lithosphere–asthenosphere p-wave reflectivity across australia. *Earth and Planetary Science Letters*, *431*, 225 - 235. Retrieved from http://www.sciencedirect.com/science/article/pii/S0012821X15006147 doi: https://doi.org/10.1016/j.epsl.2015.09.039

Kramer, S. (1996). *Geotechnical Earthquake Engineering.* Prentice Hall PTR.

Lellouch, A., Yuan, S., Spica, Z., Biondi, B., & Ellsworth, W. L. (2019). Seismic velocity estimation using passive downhole distributed acoustic sensing records: Examples from the san andreas fault observatory at depth. *J. Geophys. Res. Solid Earth*, *124*(7), 6931-6948. Retrieved from https://agupubs.onlinelibrary.wiley.com/doi/abs/10.1029/2019JB017533 doi: https://doi.org/10.1029/2019JB017533

Lobkis, O. I., & Weaver, R. L. (2003, Jun). Coda-wave interferometry in finite solids: Recovery of p-to-s conversion rates in an elastodynamic billiard. *Phys. Rev. Lett.*, *90*, 254302. Retrieved from https://link.aps.org/doi/10.1103/PhysRevLett.90.254302 doi: 10.1103/PhysRevLett.90.254302

Lyakhovsky, V., Hamiel, Y., Ampuero, J.-P., & Ben-Zion, Y. (2009, 08). Non-linear damage rheology and wave resonance in rocks. *Geophys. J. Int.*, *178*(2), 910-920. Retrieved from https://doi.org/10.1111/j.1365-246X.2009.04205.x doi: 10.1111/j.1365-246X.2009.04205.x

Martin, E. R., Lindsey, N. J., Ajo-Franklin, J. B., & Biondi, B. L. (2021). Introduction to interferometry of fiber-optic strain measurements. In *Distributed acoustic sensing in geophysics* (p. 111-129). American Geophysical Union (AGU). Retrieved from https://agupubs.onlinelibrary.wiley.com/doi/abs/10.1002/9781119521808.ch9 doi: https://doi.org/10.1002/9781119521808.ch9

Mellors, R., Kilb, D., & Ajo-Franklin, J. B. (2022). An examination of das as a possible earthquake early warning tool. In S. R. Letters (Ed.), *2022 seismological society of america annual meeting, technical sessions.* Seismological Society of America. Retrieved from https://meetings.seismosoc.org/wp-content/uploads/2022/04/SRL2B.pdf

Minato, S., Tsuji, T., Ohmi, S., & Matsuoka, T. (2012). Monitoring seismic velocity change caused by the 2011 tohoku-oki earthquake using ambient noise records. *Geophys. Res. Lett.*, *39*, L09309. Retrieved from http://dx.doi.org/10.1029/2012GL051405 doi: 10.1029/2012GL051405

Nakahara, H. (2015). Auto correlation analysis of coda waves from local earthquakes for detecting temporal changes in shallow subsurface structures: the 2011 tohoku-oki, japan earthquake. *Pure Appl. Geophys.*, *172*, 213–224. Retrieved from http://dx.doi.org/10.1007/s00024-014-0849-0 doi: 10.1007/s00024-014-0849-0

Nakata, N., & Snieder, R. (2011). Near-surface weakening in japan after the 2011 tohoku-oki earthquake. *Geophys. Res. Lett.*, *38*, L17302. Retrieved from http://dx.doi.org/10.1029/2011GL048800 doi: 10.1029/2011GL048800

Ohmi, S., Hirahara, K., Wada, H., & Ito, K. (2008). Temporal variations of crustal structure in the source region of the 2007 noto hanto earthquake, central japan, with passive image interferometry. *Earth, Planets and Space*, *60*(10), 1069–1074. Retrieved from https://doi.org/10.1186/BF03352871 doi: 10.1186/BF03352871

Ohsaki, Y. (1966). Niigata earthquakes, 1964 building damage and soil condition. *Soils and Foundations*, *6*(2), 14-37. Retrieved from https://www.sciencedirect.com/science/article/pii/S0038080620326160 doi: https://doi.org/10.3208/sandf1960.6.2_14

Ostrovsky, L., & Johnson, P. (2001). Dynamic nonlinear elasticity in geomaterials. *Rivista del nuovo cimento*, *24*(7), 1–46.

Pasqualini, D., Heitmann, K., TenCate, J. A., Habib, S., Higdon, D., & Johnson, P. A. (2007). Nonequilibrium and nonlinear dynamics in berea and fontainebleau sandstones: Low-strain regime. *J. Geophys. Res. Solid Earth*, *112*(B1). Retrieved from https://agupubs.onlinelibrary.wiley.com/doi/abs/10.1029/2006JB004264 doi: https://doi.org/10.1029/2006JB004264

Pham, T.-S., & Tkalčić, H. (2017). On the feasibility and use of teleseismic p wave coda autocorrelation for mapping shallow seismic discontinuities. *J. Geophys. Res. Solid Earth*, *122*, 3776-3791. doi: 10.1002/2017JB013975

Qin, L., Ben-Zion, Y., Bonilla, L. F., & Steidl, J. H. (2020). Imaging and monitoring temporal changes of shallow seismic velocities at the garner valley near anza, california, following the m7.2 2010 el mayor-cucapah earthquake. *J. Geophys. Res. Solid Earth*, *125*(1), e2019JB018070. (e2019JB018070 2019JB018070) doi: https://doi.org/10.1029/2019JB018070

Quigley, M. C., Bastin, S., & Bradley, B. A. (2013). Recurrent liquefaction in christchurch, new zealand, during the canterbury earthquake sequence. *Geology*, *41*, 419. Retrieved from +http://dx.doi.org/10.1130/G33944.1 doi: 10.1130/G33944.1

Régnier, J., Cadet, H., Bonilla, L. F., Bertrand, E., & Semblat, J. (2013). Assessing nonlinear behavior of soils in seismic site response: Statistical analysis on kik-net strong-motion data assessing nonlinear behavior of soils in seismic site response. *Bull. Seismol. Soc. Am.*, *103*, 1750. Retrieved from +http://dx.doi.org/10.1785/0120120240 doi: 10.1785/0120120240

Remillieux, M. C., Ulrich, T. J., Goodman, H. E., & Ten Cate, J. A. (2017). Propagation of a finite-amplitude elastic pulse in a bar of berea sandstone: A detailed look at the mechanisms of classical nonlinearity, hysteresis, and nonequilibrium dynamics. *J. Geophys. Res. Solid Earth*, *122*(11), 8892-8909. Retrieved from https://agupubs.onlinelibrary.wiley.com/doi/abs/10.1002/2017JB014258 doi: https://doi.org/10.1002/2017JB014258

Sanchez-Sesma, F. J. (1987). Site effects on strong ground motion. *Soil Dynamics and Earthquake Engineering*, *6*(2), 124-132. Retrieved from https://www.sciencedirect.com/science/article/pii/0267726187900224 doi: https://doi.org/10.1016/0267-7261(87)90022-4

Sawazaki, K., Sato, H., Nakahara, H., & Nishimura, T. (2006). Temporal change in site response caused by earthquake strong motion as revealed from coda spectral ratio measurement. *Geophys. Res. Lett.*, *33*(21). Retrieved from https://agupubs.onlinelibrary.wiley.com/doi/abs/10.1029/2006GL027938 doi: https://doi.org/10.1029/2006GL027938

Saygin, E., Cummins, P. R., & Lumley, D. (2017). Retrieval of the P wave reflectivity response from autocorrelation of seismic noise: Jakarta Basin, Indonesia. *Geophys. Res. Lett.*, *44*, 792–799. doi: 10.1002/2016GL071363

Schimmel, M., & Paulssen, H. (1997, 08). Noise reduction and detection of weak, coherent signals through phase-weighted stacks. *Geophys. J. Int.*, *130*, 497-505. doi: 10.1111/j.1365-246X.1997.tb05664.x

Sens-Schönfelder, C., & Wegler, U. (2006). Passive image interferometry and seasonal variations of seismic velocities at merapi volcano, indonesia. *Geophys. Res. Lett.*, *33*, L21302. Retrieved from `http://dx.doi.org/10.1029/2006GL027797` doi: 10.1029/2006GL027797

Shinohara, M., Yamada, T., Akuhara, T., Mochizuki, K., & Sakai, S. (2022). Performance of seismic observation by distributed acoustic sensing technology using a seafloor cable off sanriku, japan. *Front. Mar. Sci.*. doi: https://doi.org/10.3389/fmars.2022.844506

Shinohara, M., Yamada, T., Uehira, K., Sakai, S., Shiobara, H., & Kanazawa, T. (2021). Development and operation of an ocean bottom cable seismic and tsunami (obcst) observation system in the source region of the tohoku-oki earthquake. *Earth and Space Science*, *8*(3), e2020EA001359. Retrieved from `https://agupubs.onlinelibrary.wiley.com/doi/abs/10.1029/2020EA001359` (e2020EA001359 2020EA001359) doi: https://doi.org/10.1029/2020EA001359

Spica, Z. J., Castellanos, J. C., Viens, L., Nishida, K., Akuhara, T., Shinohara, M., & Yamada, T. (2022). Subsurface imaging with ocean-bottom distributed acoustic sensing and water phases reverberations. *Geophys. Res. Lett.*, *49*(2), e2021GL095287. doi: https://doi.org/10.1029/2021GL095287

Spica, Z. J., Nishida, K., Akuhara, T., Pétrélis, F., Shinohara, M., & Yamada, T. (2020). Marine sediment characterized by ocean-bottom fiber-optic seismology. *Geophys. Res. Lett.*, *47*(16), e2020GL088360. (e2020GL088360 10.1029/2020GL088360) doi: https://doi.org/10.1029/2020GL088360

Takagi, R., Okada, T., Nakahara, H., Umino, N., & Hasegawa, A. (2012). Coseismic velocity change in and around the focal region of the 2008 Iwate-Miyagi Nairiku earthquake. *J. Geophys. Res. Solid Earth*, *117*, B06315. doi: 10.1029/2012JB009252

TenCate, J. A., Pasqualini, D., Habib, S., Heitmann, K., Higdon, D., & Johnson, P. A. (2004, Aug). Nonlinear and nonequilibrium dynamics in geomaterials. *Phys. Rev. Lett.*, *93*, 065501. Retrieved from `https://link.aps.org/doi/10.1103/PhysRevLett.93.065501` doi: 10.1103/PhysRevLett.93.065501

Tork Qashqai, M., Saygin, E., & Kennett, B. (2019). Crustal imaging with Bayesian inversion of teleseismic P wave coda autocorrelation. *Journal of Geophysical Research: Solid Earth*, *124*(6), 5888–5906.

Ventosa, S., Schimmel, M., & Stutzmann, E. (2019, 05). Towards the Processing of Large Data Volumes with Phase Cross-Correlation. *Seism. Res. Lett.*, *90*(4), 1663-1669. Retrieved from `https://doi.org/10.1785/0220190022` doi: 10.1785/0220190022

Viens, L., Denolle, M. A., Hirata, N., & Nakagawa, S. (2018). Complex near-surface rheology inferred from the response of greater tokyo to strong ground motions. *J. Geophys. Res. Solid Earth*, *123*, 5710-5729. Retrieved from `https://agupubs.onlinelibrary.wiley.com/doi/abs/10.1029/2018JB015697` doi: 10.1029/2018JB015697

Viens, L., Jiang, C., & Denolle, M. A. (2022, 04). Imaging the Kanto Basin seismic basement with earthquake and noise autocorrelation functions. *Geophys. J. Int.*, *230*(2), 1080-1091. Retrieved from `https://doi.org/10.1093/gji/ggac101` doi: 10.1093/gji/ggac101

Viens, L., Perton, M., Spica, Z. J., Nishida, K., Shinohara, M., & Tomoaki, Y. (2022). *Understanding surface-wave modal content for high-resolution imaging of submarine sediments with distributed acoustic sensing.* Retrieved from `https://doi.org/10.31223/X5MW7M` doi: 10.31223/X5MW7M

Wang, H. F., Zeng, X., Miller, D. E., Fratta, D., Feigl, K. L., Thurber, C. H., & Mellors, R. J. (2018, 03). Ground motion response to an ML 4.3 earthquake using co-located distributed acoustic sensing and seismometer arrays. *Geophys. J. Int.*, *213*(3), 2020-2036. doi: 10.1093/gji/ggy102

Wapenaar, K. (2003). Synthesis of an inhomogeneous medium from its acoustic transmission response. *Geophysics*, *68*, 1756–1759. doi: https://doi.org/10.1190/1.1620649

Wegler, U., Nakahara, H., Sens-Schönfelder, C., Korn, M., & Shiomi, K. (2009). Sudden drop of seismic velocity after the 2004 mw 6.6 mid-niigata earthquake, japan, observed with passive image interferometry. *J. Geophys. Res. Solid Earth*, *114*, B06305. Retrieved from `http://dx.doi.org/10.1029/2008JB005869` doi: 10.1029/2008JB005869

Wen, K.-L., Beresnev, I. A., & Yeh, Y. T. (1995). Investigation of non-linear site amplification at two downhole strong ground motion arrays in taiwan. *Earthquake Engineering & Structural Dynamics Structural Dynamics*, *24*, 313–324. Retrieved from `http://dx.doi.org/10.1002/eqe.4290240302` doi: 10.1002/eqe.4290240302

Yates, A. S., Savage, M. K., Jolly, A. D., Caudron, C., & Hamling, I. J. (2019). Volcanic, coseismic, and seasonal changes detected at white island (whakaari) volcano, new zealand, using seismic ambient noise. *Geophys. Res. Lett.*, *46*(1), 99-108. Retrieved from `https://agupubs.onlinelibrary.wiley.com/doi/abs/10.1029/2018GL080580` doi: https://doi.org/10.1029/2018GL080580

Zaitsev, V. Y., Nazarov, V. E., Tournat, V., Gusev, V. E., & Castagnede, B. (2005). Luxemburg-gorky effect in a granular medium: Probing perturbations of the material state via cross-modulation of elastic waves. *Europhysics Letters*, *70*, 607. Retrieved from `http://stacks.iop.org/0295-5075/70/i=5/a=607`

Zeng, X., Lancelle, C., Thurber, C., Fratta, D., Wang, H., Lord, N., … Clarke, A. (2017, 01). Properties of Noise Cross-Correlation Functions Obtained from a Distributed Acoustic Sensing Array at Garner Valley, California. *Bull. Seismol. Soc. Am.*, *107*(2), 603-610. Retrieved from `https://doi.org/10.1785/0120160168` doi: 10.1785/0120160168